Available online at www.sciencedirect.com

ScienceDirect

Scripta Materialia 98 (2015) 40–43

Scripta MATERIALIA

www.elsevier.com/locate/scriptamat

Plasticity of a scandium-based nanoglass

Xiao Lei Wang,[a] Feng Jiang,[a,*] Horst Hahn,[b,e] Ju Li,[c,d,*] Herbert Gleiter,[b,e] Jun Sun[a] and Ji Xiang Fang[a,*]

[a]*State Key Laboratory for Mechanical Behavior of Materials, School of Materials Science and Engineering, School of Science, Xi'an Jiaotong University, Shaanxi 710049, People's Republic of China*

[b]*Institute for Nanotechnology, Karlsruhe Institute of Technology (KIT), Karlsruhe 76021, Germany*

[c]*Department of Nuclear Science and Engineering, MIT, Cambridge, MA 02139, USA*

[d]*Department of Materials Science and Engineering, MIT, Cambridge, MA 02139, USA*

[e]*Herbert Gleiter Institute of Nanoscience, Nanjing University of Science and Technology, Nanjing, Jiangsu 210094, People's Republic of China*

Received 28 September 2014; revised 9 November 2014; accepted 9 November 2014
Available online 1 December 2014

The mechanical properties of a $Sc_{75}Fe_{25}$ nanoglass and monolithic metallic glass (MG) with identical chemical composition were investigated by means of nanoindentation tests and quantitative in situ compression tests and tensile tests in a transmission electron microscope. The nanoglass exhibits excellent plastic deformation ability relative to the monolithic MG. It is particularly interesting to find that the 400 nm $Sc_{75}Fe_{25}$ nanoglass exhibits a 15% plastic strain under uniaxial tension. Such a nearly uniform tensile plasticity is unprecedented among MGs of similar sample sizes. The enhanced plasticity of the nanoglass can be attributed to its unique microstructure.

Keywords: Nanoglass; Glass–glass interface; Plasticity; In situ TEM

Nanoglasses, a new type of amorphous material with an inhomogeneous microstructure, were first proposed by Jing et al. in 1989 [1]. So far, nanoglasses have been produced by consolidating nanometer-sized glassy clusters [2], magnetron sputtering using powder targets [3] or electrochemical transformation [4]. The microstructure of nanoglasses consists of nanoscaled (<100 nm) contiguous glassy regions (grains) and glass–glass interfaces (GGIs) between these regions. The GGI is usually about one or several nanometers wide with a locally reduced density relative to the densities in the interior of the glassy grains [2,3,5]. The difference in the density of grains and interfaces induces a bimodal distribution of free volume in the nanoglass [2]. Preliminary investigations have shown that nanoglasses present enhanced catalytic activity [3], different magnetic properties [6], remarkable biocompatibility [7] and ultrastable kinetic behavior [8] when compared with chemically identical monolithic metallic glasses (MGs). These novel features of nanoglasses seem to open the way for new technological applications of MGs. Furthermore, nanoglasses show enhanced plasticity due to multiple shear banding [2,9]. However, the underlying mechanism is not clear, and needs further experimental investigation. In this paper, a $Sc_{75}Fe_{25}$ nanoglass was selected as the model material. It is found that the nanoglass exhibited excellent plastic deformation ability (tensile plasticity in particular) relative to a monolithic MG with identical chemical composition, which usually has zero tensile plasticity. This enhanced plasticity is thought to be due to the unique microstructure of the nanoglass.

The $Sc_{75}Fe_{25}$ nanoglass specimens were produced by inert-gas condensation (IGC) [2], and consist of hard zones (glassy grain of diameter D of ~10 nm) with low free volume and soft zones (GGI ~1 nm thick) with high free volume, and increased potential energy [9]. The structure of the nanoglasses can be tuned by varying the size of the glassy regions or the thickness of the GGIs. A study of the atomic structure of this nanoglass and its structural evolution during annealing can be found in Ref. [2]. For comparison, ribbons of a monolithic MG with an identical chemical composition were prepared by melt-spinning.

The mechanical properties of the present nanoglass were investigated by means of nanoindentations and quantitative in situ compression/tension in a transmission electron microscope (TEM). In small-scale tests, the porosity introduced by IGC can be avoided and the mechanical properties related to the microstructure can be investigated in detail. Nanoindentations were carried out using a nanoindenter (TI950, Hysitron Inc., USA) with a Berkovich indenter. All indentation tests were performed to a peak

* Corresponding authors; e-mail addresses: jiangfeng@mail.xjtu.edu.cn; liju@mit.edu; jxfang@mail.xjtu.edu.cn

http://dx.doi.org/10.1016/j.scriptamat.2014.11.010
1359-6462/

load of 10 mN at different loading rates (10, 100 and 1000 μN s^{-1}).

A set of square taper-free pillars with nominal sizes of 300 nm (for compression tests) and 400 nm (for tensile tests) of a $Sc_{75}Fe_{25}$ nanoglass and of a monolithic MG were fabricated by focused ion beam (FIB) techniques. The 300 nm compressive pillars with a cross-section of square and an aspect ratio of ~2 were fabricated using a FEI Helios NanoLab 600i dual-beam FIB system. The tensile sample gauge was trimmed to approach the designed width (~400 nm), length (~1600 nm) and thickness (~400 nm). In situ experiments were performed inside the chamber of a JEOL JEM-2100F TEM, using a Hysitron PI95 TEM Pico-Indenter with a 2 μm diamond flat punch (for compression tests) or a tungsten grip (for tensile tests) that was fabricated using FIB, under displacement-controlled mode with a constant value 2 nm s^{-1} (nominal strain rate ~1×10^{-3} s^{-1}). The data acquisition rate was about 200 points s^{-1}. The fabrication method and test method of tensile tests is similar to that used by Tian et al. [10].

Figure 1 displays the nanoindentation load–displacement (P–h) curves for the nanoglass as well as for the monolithic MG. Only the loading portions of the P–h curves are shown. The origin of each P–h curve has been displaced for clarity. Usually, the P–h curves of MGs are segmented due to numerous discrete bursts of rapid displacements at nearly constant load (Fig. 1a), while at various loading rates, no bursts of rapid displacement were observed in the curves of the nanoglass (Fig. 1b). These behaviors (discrete bursts of rapid displacements) are analogous to the serrated flow that has been reported for various MGs in compression tests [11]. Each serration corresponds to the nucleation and growth of one shear band. With increasing loading rate, the serrated flow changes from small step-like P–h curves (at low rates) to relatively smooth curves. This change agrees with the observations reported for various MGs such as in Pd–Ni–P and Mg–Cu–Gd [12]. The absence of discrete bursts of rapid displacements in the P–h curves suggests that the nanoglass might deform uniformly by numerous shear bands being activated simultaneously. The deformation features noted at the free surfaces of the nanoglass and monolithic MG under plastic indentation can be seen in the insets of Figure 1a and b, respectively. The shape of the indent observed in the nanoglass is similar to that observed in ductile materials with material pileup mounds near the indent, whereas the indent shape of the MG appears to be similar to that in brittle materials.

In order to investigate the processes involved in the deformation of the nanoglass in comparison to the monolithic MG, quantitative in situ compression tests and tensile

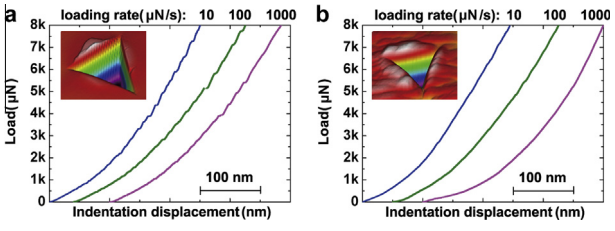

Figure 1. Typical load–displacement (P–h) curves measured at different loading rates for (a) $Sc_{75}Fe_{25}$ monolithic MG, and (b) $Sc_{75}Fe_{25}$ nanoglass. The insets of (a) and (b) are the SPM surface features for monolithic MG and nanoglass after nanoindentation, respectively.

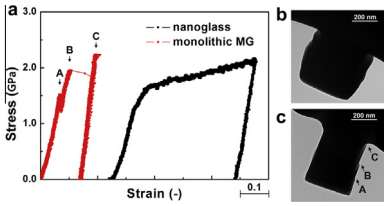

Figure 2. (a) The compressive stress–strain curves of the nanoglass and the monolithic MG; post-mortem TEM pictures of (b) nanoglass pillar and (c) monolithic MG pillar.

tests were performed for both the nanoglass and the monolithic MG in a TEM. The compressive stress–strain curves are shown in Figure 2a. In the case of the 300 nm nanoglass, the initial linear elastic deformation was followed by a plastic yield. As the plastic deformation process went on, the stress increased to ~1.27 GPa and no large stress drops were observed until the test was stopped at a pre-selected strain of 50%. Numerous small stress drops with amplitudes of <0.1 GPa were noted during the deformation of the nanoglass. Although not every shear band can be identified in the movie, these stress drops should originate from the propagation of a large number of smaller shear bands [11]. It is suggested that the nanoglass sample deformed uniformly due to multiple shear band mechanism rather than localized shear. The plastic strain was ~43% in the axial direction and ~35% in the transverse direction (Fig. 2b). The monolithic MG pillar exhibited purely elastic behavior until a stress drop with an amplitude of ~0.3 GPa occurred while the stress goes up to ~1.53 GPa (corresponding to the burst at point A in Fig. 2a). This stress drop was correlated with an obvious shear offset appearing on the free surface of pillar (point A in Fig. 2c), followed by another catastrophic stress drops (point B in Fig. 2a and c). The entire deformation processes of two samples can be found in the online Supplementary Information (Movies 1 and 2, respectively).

The tensile stress–strain curves of the nanoglass and the monolithic MG are shown in Figure 3a. The nanoglass deformed like a ductile material. It displayed significant plasticity after the yield point and before final failure. The entire tension process can be seen in Movie 3. Numerous small shear banding events corresponding to small stress drops in stress–strain curves can be seen during the deformation of the nanoglass. Whether or not the plastic deformation counts as uniform depends on the time/load/spatial resolutions of the instrument [13].

Several snapshots from this movie are displayed in Figure 3c. These snapshots correspond to points 1–6 on the stress–strain curve. At the beginning of the deformation process, the stress–strain relationship was linear. The nanoglass yielded at a stress of ~1.3 GPa and at a strain of 5.2%. Subsequently it softened and continued to undergo plastic deformation. After a uniform plastic deformation of about 6.2% (total strain 11.4% at point 4), an obvious necking in the gauge length appeared. Finally, a total strain of 18% was obtained when the in situ tensile test was stopped at a pre-selected tensile displacement. After unloading, elastic deformation recovered and a plastic strain of 15.6% was retained. The scanning electron microscopy (SEM) image of the as-deformed sample revealed the formation of a gradual neck in the gauge length due to the significant plastic deformation as shown in Figure 3d. The enlarged SEM image indicated a plastic strain of at least 15% in the axial

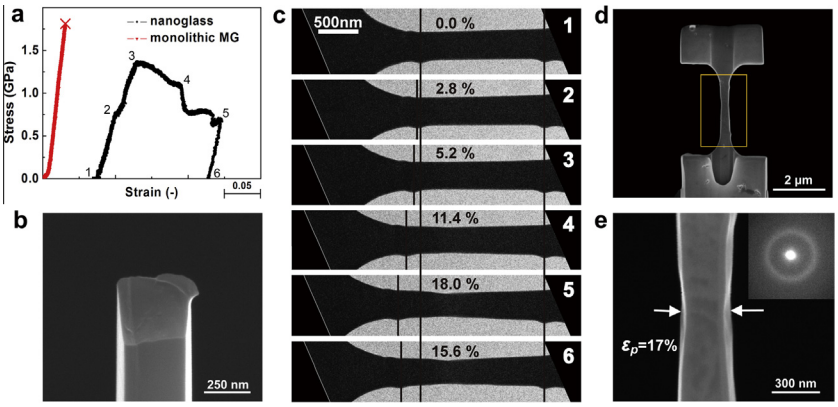

Figure 3. (a) The tensile stress–strain curves of the nanoglass and the monolithic MG; (b) tensile sample of the monolithic MG after test; (c) frames extracted from the recorded movie; (d,e) tensile sample of nanoglass after test. The inset of (e) is the corresponding selected-area diffraction pattern.

direction and ~17% in the transverse direction as shown in Figure 4e. The HRTEM selected-area diffraction patterns for the necking section of the specimen excluded the crystallization during the deformation (Fig. 3e inset). Unlike this ductile fracture behavior of nanoglass, the monolithic MG fails in a brittle manner as usual. It displayed an initially elastic deformation behavior and fractured at a stress of 1.8 GPa without any measurable plastic deformation (Movie 4). The sample failed along a ~45° shear plane, and the fracture surface was found to be featureless on the scale of SEM observation (Fig. 3b) rather than the core and vein patterns seen in bulk metallic glasses (BMGs) when these fail under tensile stress [14–16].

The nanoglass deformed more uniformly due to multiple shear banding and displayed significant plasticity. In contrast, the same sized monolithic MG fractured in a brittle manner with a single shear band. It is noted that the homogeneous deformation and enhanced tensile plasticity of nanoscale MG could be introduced by the ion irradiation during FIB preparation and e-beam damage in in-situ observation by increasing the fictive temperature of the MG [17]. These effects of ion irradiation can be ruled out because the present monolithic MG, which was subject to the same preparation and testing as the nanoglass, indeed exhibits different results. Furthermore, the nanoglass displays outstanding plasticity at a sample size that is larger than the "ductilization sample size" for the other monolithic MG (~100 nm in tensile tests [18,19] and 100–300 nm in compression tests [13,20,21]). Moreover, the entire gauge length of the nanoglass sample contributed to the plastic strain rather than only the necking region [18] (Fig. 3e). Therefore, it is proposed that the change in the mechanical behavior of nanoglass compared to the monolithic MG is due to its unique microstructure.

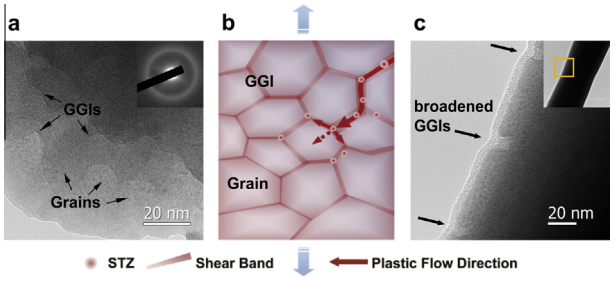

Figure 4. Schematic of the deformation process and TEM images for the nanoglass before and after deformation. (a) High-resolution TEM image of an undeformed nanoglass; the inset is the selected-area diffraction pattern recorded from the region shown in (a). (b) Shear in the nanoglass initiates in soft zones (GGIs). The propagation of the GGI flow defect will be impeded by the hard zones (glassy grains). Plastic flow then will take place in other sites, resulting in significant global plastic strain. (c) The deformed nanoglass shows the broadened interfaces due to plastic deformation; the inset is a low-magnification image, and yellow region is shown in (c). (For interpretation of color in Figure 4, the reader is referred to the web version of this article)

The microstructure of the nanoglass consisting of glassy grains of diameter D of ~10 nm and a GGI ~1 nm thick is shown in Figure 4a. These GGIs and the glassy grains are referred to as soft zones and hard zones, respectively, because the former has a much higher free volume concentration than the later. It should be noted that, in addition to GGIs, there are triple junctions among the glassy grains. Here, the triple junction is still much smaller than glassy grain and has similar size as the thickness of the GGI. Therefore, the GGIs and the triple junctions are both called GGIs for simplicity.

Upon loading, the plastic flow of MGs that occurs as a result of a series of flow defects (i.e. shear transformation zone (STZ)) will initiate stochastically but independently from fertile sites where there is usually an abundance of free volume. As the requirements for barrier energy [22] and orientations [23] have been met, a series of STZs shear cooperatively to generate a larger flow defect (embryonic shear band). When a critical incubation size scale l_{inc} is reached, the embryonic shear band will develop into a mature shear band. Inside the shear band, there is always shear softening due to free-volume generation and subsequently heating through elastic energy release [24–26]. Eventually, there is so much softening in one major shear band that cavitations occur inside, leading to fracture along the shear plane [27]. For the present nanoglass, its inhomogeneous microstructure readily induces STZs to initiate in a small subset of the soft GGIs where the Schmid factor is the largest. Soon after it initiates, the flow defect (STZs or embryonic shear band) in the GGI grows to approach the size of the glassy grain, where it will be impeded by the harder grain with less free volume. Thus the size of flow defect is limited by D, where D is the grain size of the nanoglass. If far-field stress is kept constant, the flow defect either has to penetrate the grain, or deflect the sliding to another GGI with less optimal Schmid factor. This effectively imparts a strain-hardening mechanism, on top of the strain-softening contribution

Table 1. Movies of in situ tests.

	Samples
Movie 1	300 nm nanoglass compression test
Movie 2	300 nm monolithic metallic glass compression test
Movie 3	400 nm nanoglass tensile test
Movie 4	400 nm monolithic metallic glass tensile test

*All the movies are speeded up five times.

inside the GGI flow defect due to the creation of free volume. This would delay the catastrophic localization tendency seen in monolithic MG (where there is strain softening from the outset), and plastic flow will then occur in many soft zones, resulting in a more uniform and enhanced plastic strain. As shown in Figure 4c, the thickness of many soft zones (bright regions) has broadened, providing the evidence that the soft zones have been extensively plastically deformed to accommodate applied strain. Of course, as the deformation continues and the local stress is further increased, the stopped or new GGI flow defects may subsequently penetrate the harder grain, or deflect to another GGI. Once its size grows beyond an incubation size scale $l_{inc} > \sim 100$ nm [25], there is so much strain softening inside the shear band that the strain-hardening contribution above can no longer counteract it, and then catastrophic strain localization will start to develop as in the monolithic MG, and so failure would eventually occur in the nanoglass.

Many BMGs which are prepared by consolidating micro-sized gas-atomized glassy powders usually present poor plastic deformation ability [28–30]. The basic structural units of BMGs produced by consolidation and of the present nanoglass are both glassy regions and GGIs. The main difference lies in their sizes: the former has $D > 100$ nm and the latter has $D < 10$ nm. Mature shear band with size $l_{inc} > \sim 100$ nm [25] therefore can form in one single GGI of BMGs by consolidation, whereas it would hit a GGI deflection first in a nanoglass. Therefore, BMGs produced by consolidation will fracture in a brittle manner along a main shear band, while the nanoglass can display enhanced global plasticity. The above comparison implies that the deformation mechanism of nanoglasses is microstructure size dependent, i.e. whether the grain size is larger or less than a critical incubation size scale $l_{inc.}$ This can be also verified by the recent molecular dynamics simulation of Adibi et al. [31], who proposed that there was a drastic change in deformation mode from a single shear band to homogeneous superplastic flow with a decrease in the glassy grain size.

In summary, the nanoglass exhibits significantly enhanced plastic deformation ability. Multiple shear band formation is the dominant deformation mode, which differs from that of the monolithic MG with identical chemical composition. The unique mechanical behavior is proposed to be due to the bimodal distribution of free volume in ~10 nm sized harder grains vs. ~1 nm wide softer GGIs. This work also verified an intrinsic strategy to improve the plasticity of MGs by introducing inherent nanoscale heterogeneities, below the critical incubation size scale for an embryonic shear band to grow into a mature shear band with subsequent catastrophic strain softening (see Table 1).

We thank Dr. Lin Tian for help with sample fabrication and mechanical property tests and Dr. Minqiang Jiang for valuable discussion. The financial support from the National Natural Science Foundation of China (NSFC) under Grant Nos. 51171138, 51171139, 51321003 and Ph.D. Programs Foundation of Ministry of Education of China (No. 20110201110002, 20110201120039) are gratefully acknowledged. J.L. acknowledges support by NSF DMR-1120901. The authors are also grateful for support from the XJTU Center for Advancing Materials Performance from the Nanoscale (CAMPnano).

Supplementary data associated with this article can be found, in the online version, at http://dx.doi.org/10.1016/j.scriptamat.2014.11.010.

[1] J. Jing, A. Krämer, R. Birringer, H. Gleiter, U. Gonser, J. Non-Cryst. Solids 113 (1989) 167.
[2] J.X. Fang, U. Vainio, W. Puff, R. Würschum, X.L. Wang, D. Wang, M. Ghafari, F. Jiang, J. Sun, H. Hahn, H. Gleiter, Nano Lett. 12 (2012) 458.
[3] N. Chen, R. Frank, N. Asao, D.V. Louzguine-Luzgin, P. Sharma, J.Q. Wang, G.Q. Xie, Y. Ishikawa, N. Hatakeyama, Y.C. Lin, M. Esashi, Y. Yamamoto, A. Inoue, Acta Mater. 59 (2011) 6433.
[4] A. Kushima, X.H. Liu, G. Zhu, Z.L. Wang, J.Y. Huang, J. Li, Nano Lett. 11 (2011) 4535.
[5] N. Chen, D.V. Louzguine-Luzgin, G.Q. Xie, P. Sharma, J.H. Perepezko, M. Esashi, A.R. Yavari, A. Inoue, Nanotechnology 24 (2013) 045610.
[6] M. Ghafari, S. Kohara, H. Hahn, H. Gleiter, T. Feng, R. Witte, S. Kamali, Appl. Phys. Lett. 100 (2012) 133111.
[7] N. Chen, X. Shi, R. Witte, K.S. Nakayama, K. Ohmura, H. Wu, A. Takeuchi, H. Hahn, M. Esashi, H. Gleiter, A. Inoue, D.V. Louzguine, J. Mater. Chem. B 1 (2013) 2568.
[8] J.Q. Wang, N. Chen, P. Liu, Z. Wang, D.V. Louzguine-Luzgin, M.W. Chen, J.H. Perepezko, Acta Mater. 79 (2014) 30.
[9] D. Şopu, Y. Ritter, H. Gleiter, K. Albe, Phys. Rev. B 83 (2011) 100402(R).
[10] L. Tian, Y.Q. Cheng, Z.W. Shan, J. Li, C.C. Wang, X.D. Han, J. Sun, E. Ma, Nat. Commun. 3 (2012) 609.
[11] W.J. Wright, R. Saha, W.D. Nix, Mater. Trans. 42 (2001) 642.
[12] C.A. Schuh, A.C. Lund, T.G. Nieh, Acta Mater. 52 (2004) 5879.
[13] C.Q. Chen, Y.T. Pei, O. Kuzmin, Z.F. Zhang, E. Ma, J.T.M. De Hosson, Phys. Rev. B 83 (2011) 180201.
[14] R. Raghavan, P. Murali, U. Ramamurty, Intermetallics 14 (2006) 1051.
[15] R. Raghavan, P. Murali, U. Ramamurty, Acta Mater. 57 (2009) 3332.
[16] Z.F. Zhang, J. Eckert, L. Schultz, Acta Mater. 51 (2003) 1167.
[17] D.J. Magagnosc, G. Kumar, J. Schroers, P. Felfer, J.M. Cairney, D.S. Gianola, Acta Mater. 74 (2014) 165.
[18] L. Tian, Z.W. Shan, E. Ma, Acta Mater. 61 (2013) 4823.
[19] D.C. Jang, J.R. Greer, Nat. Mater. 9 (2010) 215.
[20] O.V. Kuzmin, Y.T. Pei, C.Q. Chen, J.T.M. De Hosson, Acta Mater. 60 (2012) 889.
[21] O.V. Kuzmin, Y.T. Pei, J.T.M. De Hosson, Scr. Mater. 67 (2012) 344.
[22] C.A. Volkert, A. Donohue, F. Spaepen, J. App. Phys. 103 (2008) 083539.
[23] M.L. Falk, C.E. Maloney, Eur. Phys. J. B 75 (2010) 405.
[24] M.Q. Jiang, L.H. Dai, Acta Mater. 59 (2011) 4525.
[25] F. Shimizu, S. Ogata, J. Li, Acta Mater. 54 (2006) 4293.
[26] Y. Chen, M.Q. Jiang, L.H. Dai, Int. J. Plast. 50 (2013) 18.
[27] P. Zhao, J. Li, Y. Wang, Int. J. Plast. 40 (2013) 1.
[28] D.J. Sordelet, E. Rozhkova, P. Huang, P.B. Wheelock, M.F. Besser, M.J. Kramer, M. Calvo-Dahlborg, U. Dahlborg, J. Mater. Res. 17 (2002) 186.
[29] T.S. Kim, J.K. Lee, H.J. Kim, J.C. Bae, Mater. Sci. Eng., A 402 (2005) 228.
[30] G. Xie, D.V. Louzguine-Luzgin, H. Kimura, A. Inoue, Appl. Phys. Lett. 90 (2007) 241902.
[31] S. Adibi, Z.D. Sha, P.S. Branicio, S.P. Joshi, Z.S. Liu, Y.W. Zhang, Appl. Phys. Lett. 103 (2013) 211905.